RSC Advances

PAPER

View Article Online
View Journal | View Issue



Cite this: *RSC Adv.*, 2016, **6**, 28419

# Selectively enhanced sensing performance for oxidizing gases based on ZnO nanoparticle-loaded electrospun $SnO_2$ nanotube heterostructures†

Kaidi Diao,‡[ab] Yunpeng Huang,‡[c] Minjie Zhou,[b] Jicheng Zhang,[b] Yongjian Tang,[b] Shuxia Wang,[a] Tianxi Liu[c] and Xudong Cui*[b]

Received 2nd February 2016
Accepted 10th March 2016

DOI: 10.1039/c6ra03061k

www.rsc.org/advances

In this work, we present gas sensors based on ZnO nanoparticle-loaded electrospun $SnO_2$ nanotube (ZnO/$SnO_2$) n–n heterostructures (HSs) synthesized by electrospinning combined with facile thermal decomposition. The sensing properties of the pristine $SnO_2$ nanotubes (NTs) and ZnO/$SnO_2$ HSs were investigated toward the representative oxidizing ($NO_2$) and reducing ($H_2$, CO) gases. Results show that the as-prepared ZnO/$SnO_2$ HSs exhibit selectively enhanced and diminished sensing performances for oxidizing and reducing gases, respectively. These phenomena are closely associated with the modulation of the local depletion layer on the surface of $SnO_2$ nanoparticles (NPs) caused by charge transfer at the heterojunctions due to work function difference. A modified grain boundary-controlled sensing mechanism is proposed to describe charge transport in sensing layers based on the contact potential barriers between nanoparticles. Our study indicates that the selection of material system and their synergism are keys to the effective design of gas sensors with semiconducting metal oxide HSs.



## 1. Introduction

Metal oxide semiconductor (MOS) resistive gas sensors have been widely used in the detection of toxic, flammable and explosive gases,[1,2] energy efficiency and emission in combustion processes,[3] healthcare,[4] environmental monitoring,[5] and food processing.[6,7] With the urgent requirements of sustainable development all over the world, gas sensing techniques are now facing challenges towards high sensitivity and selectivity, and short response and recovery times at low gas concentrations. For instance, the U.S. Environmental Protection Agency (EPA) has set a primary standard of 53 parts per billion (ppb) for $NO_2$,[8] above which may cause possible health problems especially for those sensitive populations including children, elderly and people with asthma, just naming a few critical challenges. It is therefore of crucial importance to develop high-performance gas sensors to fulfill those future missions.

Currently, various approaches have been used to approach above-mentioned goals with MOS gas sensors. These include doping or surface decorating with noble metal or metal oxide nanoparticles, compositing with other oxides, or plasma exposure *etc.*[9–16] Among them, the HSs formed by surface coating with NPs, particularly metal oxide NPs with special functionalities is a widely accepted route to improve the sensing performance.

The metal oxide NPs are considered to be electronically sensitive and can modulate the conduction channel through charge transfer at the interface between the host materials and the attached NPs.[17] Due to the modulation, the electric conduction in the sensing layer of a gas sensor becomes more sensitive to the process of gas adsorption and desorption, remarkably influencing the sensing performance. Generally, two approaches have been employed to realize charge transfer between the host materials and the attached NPs. One is the use of p–n heterojunction.[16,18–20] Due to carrier concentration gradient, charge transfer will occur at the interface until the built-in electric field is formed to prevent carrier flow and finally reaches equilibrium in the p–n heterojunction.[18] The other is the n–n or p–p isotype heterojunction, in which charge transfer occurs due to the work function difference between the host materials and the attached NPs.[19,20] From the engineering's point of view, isotype heterojunctions are preferred since constructing the work function difference is relatively easy to be implemented with a variety of materials. In this work, we then aim to n–n HSs configuration and carefully investigate the contribution of heterojunctions to the sensing performance.

One-dimensional (1D) metal oxides (*i.e.*, nanowires, nanobelts, nanorods, NTs and nanofibers, *etc.*) have been attracting intensive attentions as potential sensing materials due to their high surface-to-volume ratio and efficiencies for carrier

[a]*Department of Applied Physics, Chongqing University, Chongqing, 400044, China*
[b]*Science and Technology on Plasma Physics Laboratory, Research Center of Laser Fusion, CAEP, Mianyang, 621900, China. E-mail: xudcui@gmail.com*
[c]*State Key Laboratory of Molecular Engineering of Polymers, Department of Macromolecular Science, Fudan University, Shanghai, 200433, China*

† Electronic supplementary information (ESI) available. See DOI: 10.1039/c6ra03061k

‡ K. D. and Y. H. contribute equally to this work.

transport.[21,22] Particularly, 1D electrospun nanostructures consisting of many nanograins would result in potential barriers between the adjacent NPs, quite different from other types of 1D nanostructures.[23,24] More importantly, the potential barrier can be easily modulated by the process of gas adsorption and desorption, which ensures that the structures exhibit excellent sensing performance.[25] It has been demonstrated that the 1D electrospun nanostructures with NPs coatings can effectively improve sensor performance toward some target gases ($NH_3$, $H_2S$, $H_2$ and $NO_2$) due to the formation of local heterojunctions.[26–30] Up to date, there still have been some critical challenges left to further exploit the potentials for these structures. (1) Are the NPs-coated 1D electrospun nanostructures efficient for the target gases, regardless of their oxidizing or reducing nature? (2) How does the local heterojunction impact the potential barriers between the adjacent nanograins? (3) What is the possible sensing mechanism for the NPs-coated 1D electrospun nanostructures? To address these issues, here we select two common and typical sensing materials, $SnO_2$ and ZnO as examples. Although the single 1D electrospun nanostructures of those two materials have exhibited high sensing performance, their synergism is expected to further improve the performance and extend the applications of devices at low concentration and complex atmospheres.

In this work, we present the gas sensors based on ZnO nanoparticle-loaded electrospun $SnO_2$ NT n–n HSs synthesized by the electrospinning and thermal decomposition. The sensing properties of the pristine $SnO_2$ NTs and ZnO/$SnO_2$ HSs are investigated toward the representative oxidizing ($NO_2$) and reducing ($H_2$, CO) gases. Results show that compared with the pristine $SnO_2$ NTs, ZnO/$SnO_2$ HSs exhibit selectively enhanced and diminished sensing performances for oxidizing and reducing gases, respectively. A modified grain boundary-controlled sensing mechanism is proposed to interpret these phenomena based on the modulation of local depletion layers on surface of $SnO_2$ NPs. Our study indicates that the selection of material system and their synergism are keys to the effective design of gas sensors with semiconducting metal oxide HSs.

## 2. Experimental

### 2.1. Materials

Zinc acetate dihydrate ($Zn(CH_3COO)_2 \cdot 2H_2O$), and anhydrous ethanol were purchased from Chengdu Kelong Chemical Co. Ltd., China. Polyvinylpyrrolidone (PVP, $M_w = 1\ 300\ 000\ g\ mol^{-1}$) was obtained from Sigma-Aldrich. Tin(II) chloride dihydrate ($SnCl_2 \cdot 2H_2O$), and *N*,*N*-dimethylformamide (DMF) were supplied by Shanghai Chemical Reagent Company, China. All the chemicals were of analytical reagent grade and used without further purification. Deionized water with a resistivity of 18.25 MΩ cm was obtained using an up-water purification system (Chengdu YouPu Technology Co. Ltd., China) at room temperature.

### 2.2. Preparation of ZnO/$SnO_2$ HSs

The $SnO_2$ NTs were synthesized by electrospinning as reported in our previous work.[31] In experiments, 1.2 g $SnCl_2 \cdot 2H_2O$ was dissolved in a mixture of ethanol (5 mL) and of DMF (5 mL) with vigorous stirring at room temperature. Afterwards, 1.2 g PVP was added to the above mixture and stirred overnight to form a uniformly transparent solution. Then, the solution was transferred into a plastic syringe and injected in a rate of 0.25 mL $min^{-1}$ using a no. 21 stainless steel needle connected to a high voltage DC power supply. Here, a rotating aluminum drum was selected as the collector with a distance of ~18 cm to the needle tip. When a fixed voltage of 21 kV was applied to the system, the electrospun $SnCl_2$/PVP nanofibers were produced and deposited on the aluminum drum. Finally, the $SnCl_2$/PVP nanofibers were peeled off from the collector and calcinated for 3 h at 600 °C in air to remove the polymer and form $SnO_2$ NTs.

The ZnO/$SnO_2$ HSs were synthesized by a one-step thermal decomposition according to Zhao's method.[32] Briefly, a certain amount of saturated ethanol solution of $Zn(CH_3COO)_2 \cdot 2H_2O$ were dropped onto the dispersed $SnO_2$ NTs and dried in air. Then the zinc acetate covered $SnO_2$ NTs were baked at 450 °C for 20 min in air to obtain the ZnO/$SnO_2$ HSs.

### 2.3. Characterization

The morphology of resulting products was investigated using a FEI field emission scanning electron microscopy (FESEM) equipped with an Oxford energy dispersive X-ray spectroscopy (EDS) operated at 15 kV. The detailed microstructure of the ZnO/$SnO_2$ HSs was studied by a transmission electron microscopy (TEM) and a high-resolution transmission electron microscopy (HRTEM) performed with a FEI TEM under an accelerating voltage of 200 kV. The powder X-ray diffraction (XRD) patterns were recorded on a Bruker X-ray diffractometer with Cu K$\alpha$ radiation ($\lambda = 0.154$ nm) operating at 40 kV in the $2\theta$ range from 20° to 80°.

### 2.4. Fabrication and measurement of gas sensors

The gas sensors were fabricated by a similar method as reported in our previous work.[33] First, the as-synthesized sensing materials, including $SnO_2$ NTs and ZnO/$SnO_2$ HSs, were mixed with deionized water in a weight ratio of 4 : 1 and slightly grinded in an agate mortar to form homogeneous pastes. Then, the pastes were coated on a ceramic substrate of Au interdigitated electrode. After drying at room temperature for 24 h in air, the sensing devices were sintered at 400 °C for 2 h to improve the mechanical strength (Fig. 1 inset).

The gas-sensing properties of the sensors were investigated with a CGS-4TP intelligent gas sensing analysis system (Beijing Elite Tech Co. Ltd., China) as shown in Fig. 1. This multifunctional system consists of a heating system, a probe adjustment system, a measurement and data acquisition system, as well as a set of built-in measurement control software. An external temperature control provided by the system can conductively adjust the sensor temperature from 20 °C to about 500 °C with a precision of 1 °C. Two probes were pressed on sensor substrates to export electrical signals. All sensors were preheated at different operating temperatures for about 30 min. When the sensor resistances were stable, the target gas with a certain concentration was injected into the test chamber (1.8 L

 

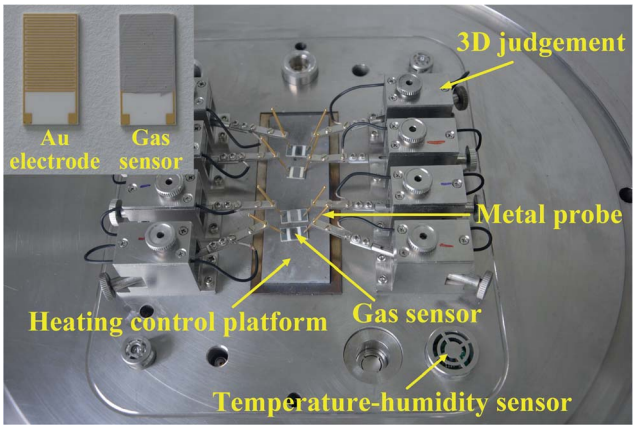


Fig. 1 Photograph of the intelligent gas sensing analysis system of CGS-4TP. The inset is a top view of Au interdigitated electrode and a sample sensor.

in volume) in 1000 standard cubic centimeters per minute (sccm) by a mass flow controller (MFC). After the sensor resistances reached new constant values, the dry air was injected into the test chamber in 1000 sccm by MFC. The operating temperature, the sensor resistance and response values of these sensors were automatically reported by the analysis system. The response value ($R$) was defined as $R = R_g/R_a$ or $R = R_a/R_g$ for the oxidizing and inducing gases, respectively, where $R_a$ was the sensor resistance in the ambient air and $R_g$ was the sensor resistance in the detected gas. The response time and recovery time were defined as the time taken for the sensor to reach 90% of its maximum response and decrease to 10% of its minimum response, respectively.

## 3. Results and discussion

### 3.1. Morphology and structure

The morphologies of the as-prepared electrospun $SnO_2$ NTs and ZnO/$SnO_2$ HSs were observed using FESEM. Fig. 2a shows a hollow tubular structure of the $SnO_2$ NTs with an outer diameter ranging from ~470 nm to ~580 nm. The surface is extremely rough, covered with nanosized $SnO_2$ grains with an average diameter of ~90 nm. The thickness of the tube wall is about 130 nm. Fig. 2b shows a low-magnification SEM image of the ZnO/$SnO_2$ HSs after thermal decomposition process. It can be seen that, the tubular structure is maintained, and the surface becomes much rougher. At higher magnification (Fig. 2c), it can be observed that many tiny ZnO NPs with a mean size of ~40 nm are loaded on the surface of $SnO_2$ NTs. The ZnO/$SnO_2$ HSs comprising of two different components are further confirmed by the EDS mapping analysis (Fig. 2d–g), confirming the existence of Zn (3.37 wt%) element besides Sn (75.45 wt%) and O (21.18 wt%) elements, where the $SnO_2$ NTs are uniformly covered with ZnO NPs. According to the EDS data, the percentage of ZnO in ZnO/$SnO_2$ HSs is 4.19 wt%. The tubular structure and rough surface of ZnO/$SnO_2$ HSs are expected to significantly increase the active sites for gas adsorption, and provide an effective way to improve gas–solid interaction.

To further analyze the detailed microstructure and morphology of ZnO/$SnO_2$ HSs, TEM and HRTEM observations were carried out. As shown in Fig. 3a and b, the TEM images confirm that the ZnO/$SnO_2$ HSs present rough tubular structure, and the tube walls are uniformly coated with tiny ZnO NPs, being consistent with the observations in FESEM images. In the HRTEM images of ZnO/$SnO_2$ HSs (Fig. 3c and d), uniform lattice fringe are observed, and the lattice fringes of $d = 0.34$ nm and 0.26 nm match well with the crystallographic planes of rutile $SnO_2$ (110) and hexagonal wurtzite ZnO (002), respectively.

In order to analyze the composition and crystalline structure, XRD measurement was then performed. As shown in Fig. 4a, high intensity diffraction peaks are indexed to pure $SnO_2$ crystals with a rutile structure, well agreeing with the reported values from the Joint Committee on Powder Diffraction Standards card (JCPDS no. 41-1445). No characteristic peaks from other impurities are observed in the XRD pattern, and the sharp diffraction peaks confirm the good crystallinity of $SnO_2$ NTs. Fig. 4b shows the XRD pattern taken from ZnO/$SnO_2$ HSs. Compared to the pure $SnO_2$ NTs, two new but relatively weak diffraction peaks at $2\theta = 31.8°$ and 36.3° are detected, which can be respectively assigned as the (100) and (101) planes of the hexagonal wurtzite ZnO (JCPDS no. 41-1451), further indicating the formation of ZnO NPs coated on the surface of $SnO_2$ NTs. According to Scherrer formula, the crystallite size is about 51.3 nm, 22.5 nm for $SnO_2$ and ZnO nanoparticles, respectively. Note that in the XRD patterns, the peak at $2\theta = 33.9°$ indexing to the (101) plane of $SnO_2$ is rather intense and slightly broaden, the diffraction peak at $2\theta = 34.4°$ assigning to the (002) plane of ZnO is overlapped and cannot be observed. Nevertheless, the (002) plane of ZnO is clearly observed in HRTEM images (Fig. 3c and d).

### 3.2. Gas-sensing performance

The operating temperature of metal oxide gas sensors plays a vital role on their sensing performance.[34,35] Generally, by elevating operating temperature, one could achieve an optimal response with improved gas–solid interaction and relatively large surface adsorption. In our work, to determine the optimal operating temperature, the temperature dependent sensing behaviors of the $SnO_2$ NTs and ZnO/$SnO_2$ HSs sensors to the target gases $NO_2$ (10 ppm), $H_2$ (50 ppm) and CO (50 ppm) are investigated at temperatures ranging from 150 °C to 400 °C. As shown in Fig. 5, the response of all sensors exhibits a trend of "increase-maximum-decay" with the operating temperature, and the largest response is found at 300 °C for all sensors. We can find that, in the initial stage, the gas chemisorption is higher than the gas desorption on the oxide surfaces at low temperature range, thus the adsorption quantity increases with the elevated temperature. As the temperature rises, the gas chemisorption will gradually decrease and the gas desorption will increase, until a balance of these two processes is reached. At this balance point, the adsorption quantity reaches a maximum, or in other words, the sensor exhibits the best response. After this critical point, the exothermic gas chemisorption becomes difficult and the gas desorption dominates,

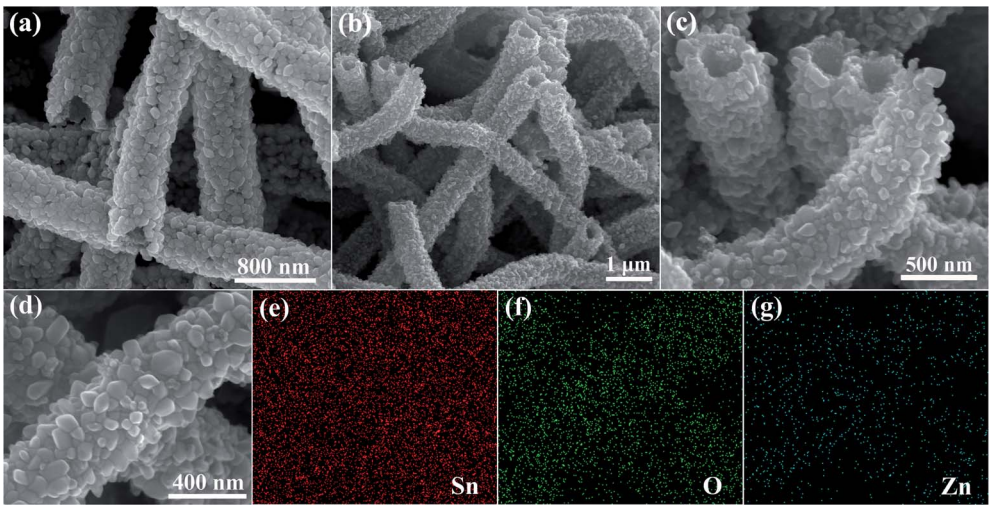


Fig. 2 FESEM images of (a) the electrospun $SnO_2$ NTs and (b and c) ZnO/$SnO_2$ HSs. (d–g) shows the EDS elemental mapping images of the ZnO/$SnO_2$ HSs.

leading to a reduced response.[36] Thus 300 °C is selected as the optimal operating temperature and all the following measurements were performed at this temperature.

The dynamic resistance behaviors of the $SnO_2$ NTs and ZnO/$SnO_2$ HSs were investigated towards a typical oxidizing gas $NO_2$. Fig. 6a shows the real-time response–recovery curves of both sensors to $NO_2$ with the concentration of 0.5–100 ppm. Once the sensors are exposed to a certain concentration of $NO_2$ in each dynamic cycle, the resistance of both sensors will increase; when the gas supply is stopped, the sensor resistance decreases and finally returns to its baseline, confirming that both sensors are with desired reversibility and repeatability. This is the characteristics of n-type semiconducting oxides to oxidizing gases, and has been well interpreted.[37] Note that from the inset of Fig. 6a, the ZnO/$SnO_2$ HSs exhibit a smaller baseline (~2.4 kΩ) than that of the $SnO_2$ NTs (~4.9 kΩ), being closely related to the modulation of ZnO NPs on the depletion layer of $SnO_2$ NPs at the local heterojunctions.[9,38] We will discuss this in next section. When focus on a certain dynamic cycle, the ZnO/$SnO_2$ HSs present a larger resistance change compared with the case of $SnO_2$ NTs, implying that a larger sensor response is achieved, especially at high gas concentrations. Fig. 6b shows the response of both sensors as a function of gas concentration from 0.5 ppm to 100 ppm. The responses of both sensors increase with gas concentration, roughly obeying linear relationship. Taking the 10 ppm $NO_2$ as an example, the ZnO/$SnO_2$ HSs has a response of 65.9, being six times higher than that of the $SnO_2$ NTs (10.6). Clearly, surface functionalization would assist to improve the response of $SnO_2$ NTs based gas sensors. Nevertheless, the response and the recovery times of the ZnO/$SnO_2$ HSs are prolonged (Fig. 6c and d). Based on the above results, we can see that the ZnO/$SnO_2$ HSs can remarkably enhance the sensor response toward the representative oxidizing gas ($NO_2$). We then look back to the first issue: is this structure also efficient for the reducing gases?

Accordingly, the sensing performance of the $SnO_2$ NTs and ZnO/$SnO_2$ HSs were investigated to the typical reducing gases $H_2$ and CO in the range of 10–50 ppm. From Fig. 7a and b, it is observed that the sensor resistances decrease when $H_2$ or CO are injected, and then reach steady values; once the gas supply is stopped, the resistances will increase and finally return to their baselines. Although the dynamic behavior of the sensors to reducing gases is completely different from the case of $NO_2$, the phenomenon can also be well explained by the sensing mechanism of n-type semiconducting oxides to reducing gases.[37] The baseline resistance of the ZnO/$SnO_2$ HSs is lower than that of $SnO_2$ NTs, being consistent with the results in the

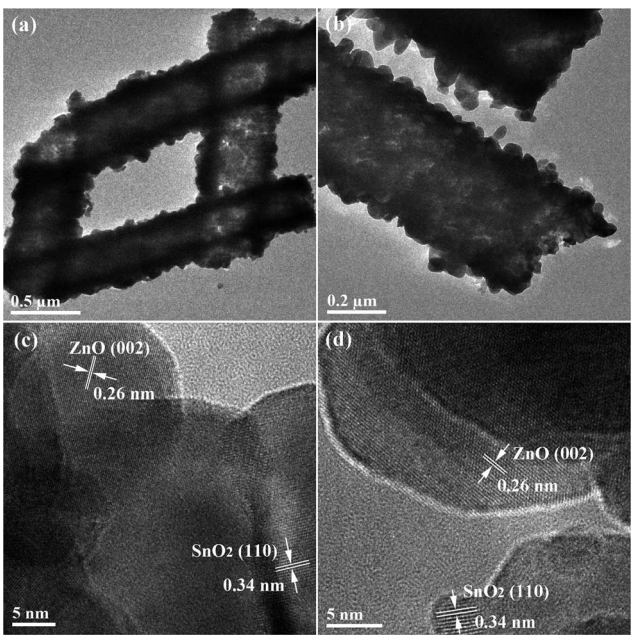


Fig. 3 Bright-field (a and b) TEM and (c and d) HRTEM images of the ZnO/$SnO_2$ HSs.

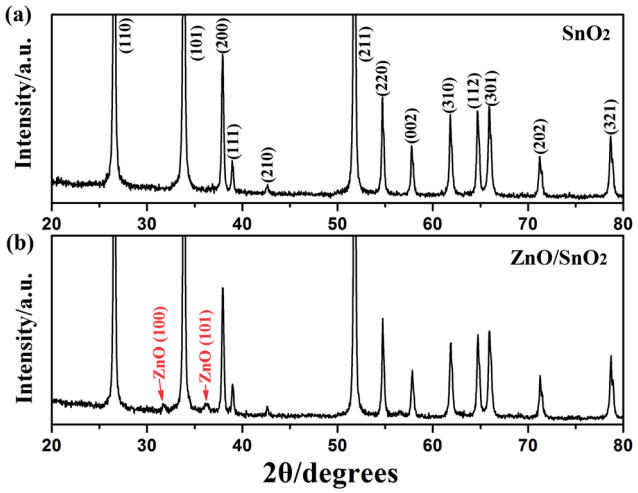


Fig. 4 XRD patterns of (a) the electrospun $SnO_2$ NTs and (b) the ZnO/$SnO_2$ HSs.

case of $NO_2$. More interestingly, the ZnO/$SnO_2$ HSs exhibit much smaller resistance change than that of $SnO_2$ NTs, being opposite to the case of $NO_2$. The resistance change of ZnO/$SnO_2$ HSs could hardly be detected at the concentration of 10 ppm for $H_2$, even for CO at 25 ppm. The change of sensor resistance is expressed as sensor response and summarized as a function of gas concentration shown in Fig. 7c and d. There exist two features: first, the sensor response roughly increases with the gas concentration; the ZnO/$SnO_2$ HSs exhibit smaller sensor response compared with the $SnO_2$ NTs. Even at high concentration of 100 ppm, the responses of ZnO/$SnO_2$ HSs are only 1.9 and 1.1 for $H_2$ and CO, respectively, indicating that the ZnO/$SnO_2$ HSs can greatly decline the sensor response to reducing gases.

In order to intuitively compare the sensing performances of the $SnO_2$ NTs and the ZnO/$SnO_2$ HSs to oxidizing and reducing gases, the sensor responses of both sensors to CO (50 ppm), $H_2$ (50 ppm) and $NO_2$ (5 ppm) are displayed in Fig. 8. For the reducing gases, the ZnO/$SnO_2$ HSs exhibit declined device response. Particularly, the response of ZnO/$SnO_2$ HSs (1.44) for $H_2$ becomes nearly one-fifth of the $SnO_2$ NTs (6.89). While for the oxidizing gas ($NO_2$), the ZnO/$SnO_2$ HSs present remarkably enhanced effect, showing six times higher response (30.84) than that of the $SnO_2$ NTs (5.09). Thanks to the opposite trend, the ZnO/$SnO_2$ HSs exhibit a excellent selectivity to $NO_2$, although the concentration of $NO_2$ is only one-tenth of the reducing gases. On the basis of this effect, we believe that our devices can be used to selectively detect oxidizing gases under complex atmospheres, in which reducing gases and oxidizing gases coexist, for instance, in chemical industries, laboratories, mines *etc.*

### 3.3. Gas-sensing mechanism

It is well known that the gas-sensing property is heavily dependent on surface area and porosity.[39] To examine these parameters, nitrogen adsorption and desorption measurements are performed on the sensor materials (Fig. S1†). The isotherms roughly belong to the type III isotherm in the IUPAC classification, and exhibit type H3 loop, indicating that all samples have similar pore size distribution, *i.e.*, average pore size of ~2–50 nm in diameter.[40] The BET surface areas of ZnO/$SnO_2$ HSs is ~5.65 $m^2$ $g^{-1}$, only a litter higher than that of the electrospun $SnO_2$ NTs (~5.54 $m^2$ $g^{-1}$). Since the difference of the BET

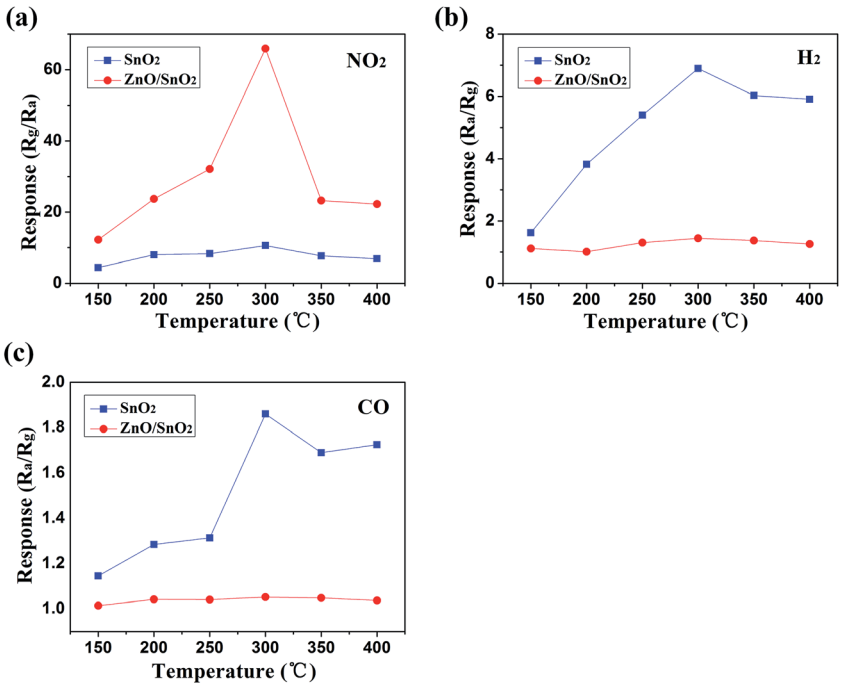


Fig. 5 Sensor responses of the electrospun $SnO_2$ NTs and ZnO/$SnO_2$ HSs at different temperatures (150–400 °C) toward (a) $NO_2$ (10 ppm), (b) $H_2$ (50 ppm) and (c) CO (50 ppm).

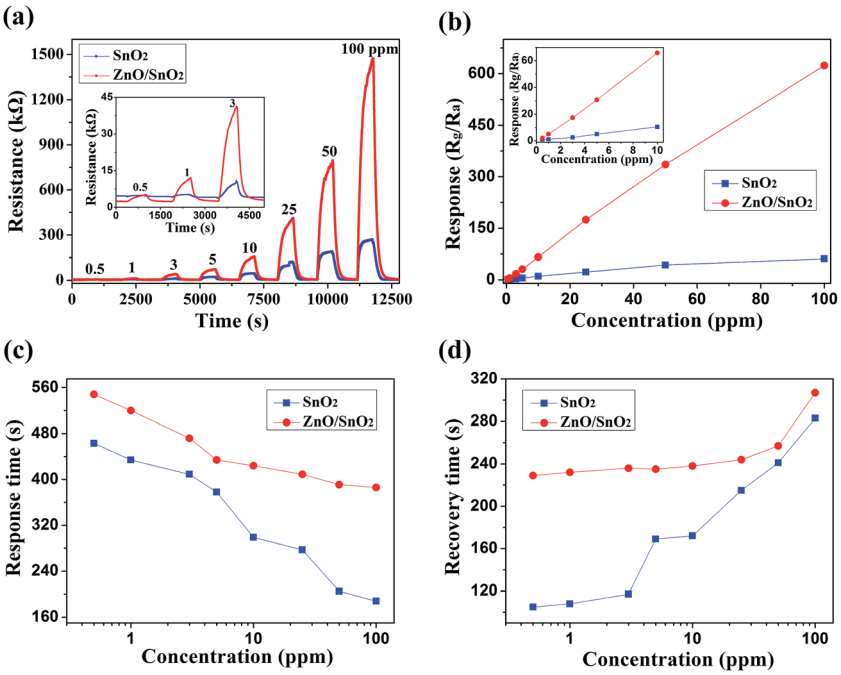


Fig. 6 Gas sensing performance of the electrospun $SnO_2$ NTs and ZnO/$SnO_2$ HSs toward $NO_2$ in concentration range of 0.5–100 ppm: (a) typical dynamic curves; (b) sensor response as a function of gas concentration; (c) response time; (d) recovery time. Inset of panel (a) shows dynamic curves in concentration range of 0.5–3 ppm. Inset of panel (b) shows sensor responses as a function of gas concentration (0.5–10 ppm).

surface area of both the samples may be negligible, we reasonably believe that the main factors leading to sensing difference should be other reasons. In addition, after surface loading of ZnO NPs on $SnO_2$ NTs, the original tubular structure is still maintained and the mean size of ZnO nanoparticles is ~40 nm, so the morphology of the ZnO/$SnO_2$ HSs is almost the same as $SnO_2$ NTs. Accordingly, the true factor resulting in the sensing difference may be the modulation of depletion layer on surface of $SnO_2$ NPs caused by charge transfer at the local heterojunctions.

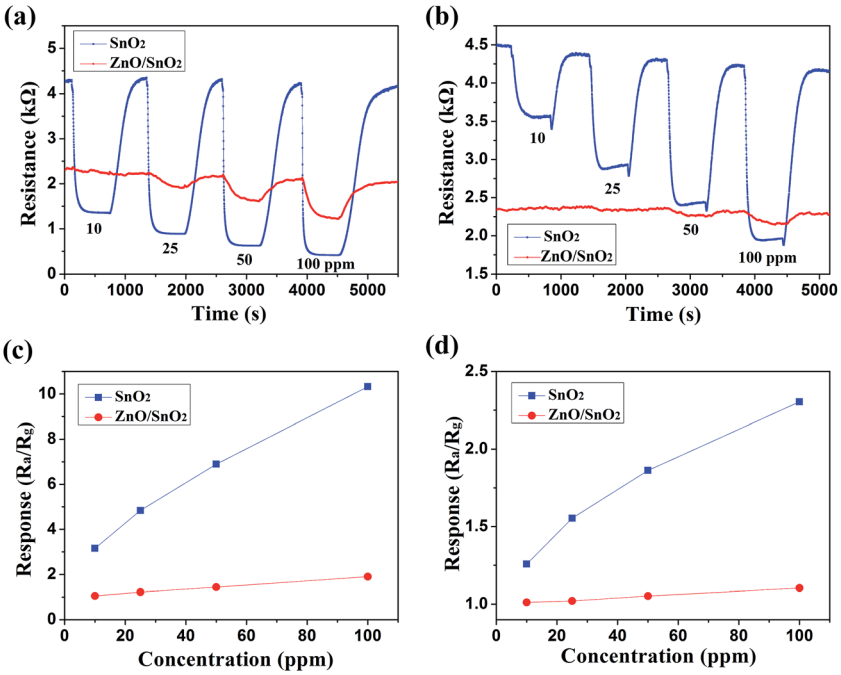


Fig. 7 Gas sensing performances of the electrospun $SnO_2$ NTs and ZnO/$SnO_2$ HSs toward $H_2$ and CO in the range of 10–100 ppm: typical dynamic curves toward (a) $H_2$ and (b) CO; sensor responses as a function of gas concentration toward (c) $H_2$ and (d) CO.

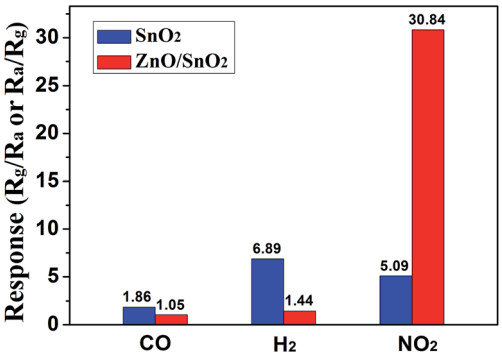


Fig. 8 Comparison of the sensor responses based on the electrospun $SnO_2$ NTs and ZnO/$SnO_2$ HSs toward CO (50 ppm), $H_2$ (50 ppm) and $NO_2$ (5 ppm).

Compared with 1D single-crystal nanowires, the tube walls of both $SnO_2$ NTs and ZnO/$SnO_2$ HSs are constructed with nano-sized $SnO_2$ grains, resulting in a large amount of homojunctions at the boundaries between the adjacent nanograins. Due to the structure characteristic of tube walls, there would be some interspaces between nanograins in sensing layers.[41–43] As shown in Fig. 9a$_1$, when the $SnO_2$ NTs sensor is exposed to the air, the oxygen molecules will diffuse into the tube walls through interspaces and surround the nanograins. Then the oxygen molecules will be chemisorbed on the surface of nanograins and become oxygen species ($O_2^-$, $O^-$ or $O^{2-}$) by extracting electrons from the conduction band of $SnO_2$ grains, resulting in an electron depletion layer on the surface of oxides.[37] At the same time, the energy band upward bends at the grain boundaries. The generated potential barriers between homojunctions will obstruct the transport of electrons under the applied voltage. Under this circumstance, the sensor will maintain the produced initial resistance, *i.e.* the baseline in air. If the sensor is exposed to the atmosphere including reducing gases (Fig. 9a$_2$), the chemisorbed oxygen species will interact with the reducing gases and being removed from the surface of the oxides. The captured electrons will return to the conduction band, and the potential barriers will decrease, resulting in a depressed sensor resistance. When the sensor is exposed to an oxidizing gas (Fig. 9a$_3$), the oxidizing gas ($NO_2$) will diffuse into the tube walls through interspaces and be chemisorbed on the surface of the nanograins, further trapping electrons from the conduction band. As a consequence, the potential barrier will increase, resulting in a larger sensor resistance.[25,44,45] In the sensing process, the modulation of potential barriers between the adjacent nanograins is key to determine the change of sensor resistance, *i.e.* the sensor response. The potential barrier is induced by the electron depletion whose width can be denoted by the Debye length ($\lambda_D$). The Debye length of an oxide material can be expressed by the following equation:[46]

$$\lambda_D = \sqrt{\frac{\varepsilon kT}{q^2 n_c}},$$

where $\varepsilon$ is the static dielectric constant, $k$ is the Boltzmann's constant, $T$ is the absolute temperature, $q$ is the electrical charge and $n_c$ is the carrier concentration. For the $SnO_2$ NTs, the Debye length is calculated to be ~3.2 nm with $\varepsilon = 13.5 \times 8.85 \times 10^{-12}$ F m$^{-1}$, $T = 573$ K, $n_c = 3.6 \times 10^{18}$ cm$^{-3}$.[47] In principle, for the pure $SnO_2$ NTs, the width of the depletion layer could be expanded or compressed due to the change of electron concentration caused by oxidizing and reducing gases, which eventually determine the potential barriers between the adjacent nanograins.

When ZnO NPs are attached on the surface of $SnO_2$ NTs (Fig. 9b), there exist two physical phenomena. One occurs on the surface of ZnO NPs due to gas adsorption, and the other is at the interface between the ZnO NPs and $SnO_2$ NPs. When the ZnO/$SnO_2$ HSs is exposed in air (Fig. 9b$_1$), oxygen molecules are chemisorbed on the surface of ZnO NPs, then the gas molecules will capture electrons from the conduction band of ZnO NPs, resulting in electron depletion.[37] The width of electron depletion layer can also be indicated by the Debye length. For ZnO

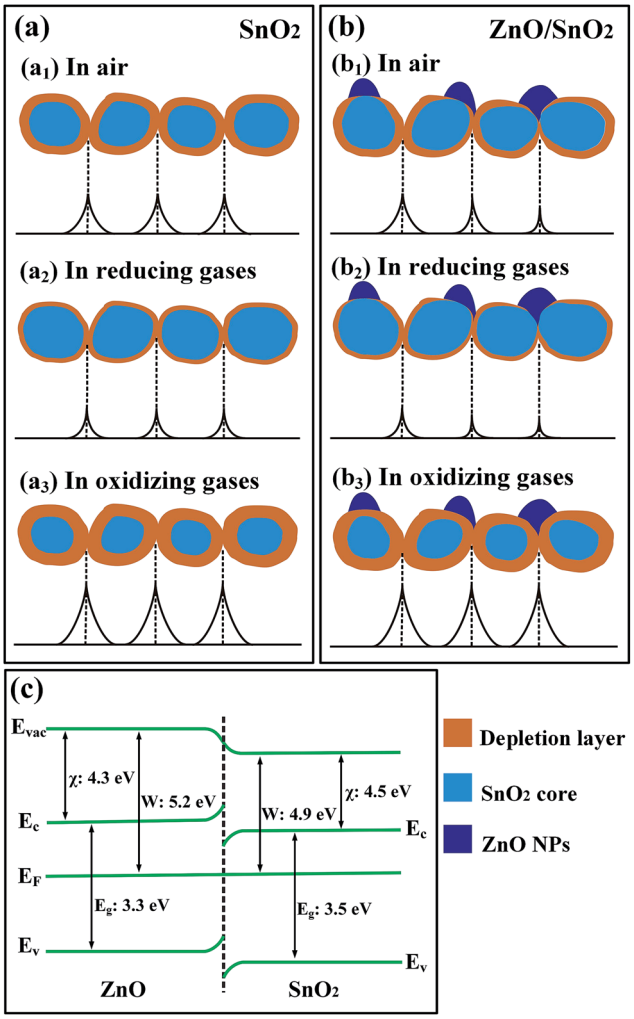


Fig. 9 Schematically showing the modulation of potential barriers between $SnO_2$ NPs to reducing and oxidizing gases based on grain boundary-controlled sensing mechanism: (a) the electrospun $SnO_2$ NTs; (b) the ZnO/$SnO_2$ HSs. (c) Energy-band diagram of ZnO/$SnO_2$ heterojunction.

NPs, $\varepsilon = 8.75 \times 8.85 \times 10^{-12}$ F m$^{-1}$,[48] $T = 573$ K, the carrier concentration varies in the range of $10^{16}$ to $10^{19}$ cm$^{-3}$,[49] thus the Debye length changes from ~22 nm to ~0.7 nm, smaller than the mean size (40 nm) of ZnO NPs. This indicates that the region of ZnO NPs close to $SnO_2$ NPs is not affected by the gas chemisorption. On the other hand, since the work function of ZnO NPs (5.2 eV) is larger than that of $SnO_2$ NPs (4.9 eV), electrons will transfer from ZnO NPs to $SnO_2$ NPs until a same Fermi level is reached (Fig. 9c). Thus, the width of depletion layer at the local heterojunctions reduces on the side of $SnO_2$. Particularly, the ZnO NPs on or close to the boundaries between the adjacent $SnO_2$ NPs can heavily decrease the potential barriers (Fig. 9b$_1$). The relatively weak potential barriers cause a small sensor baseline for the ZnO/$SnO_2$ HSs. When the sensor is exposed to the oxidizing gas (Fig. 9b$_3$), the electron depletion layer of the $SnO_2$ NPs expands to a width as wide as the pure $SnO_2$ NTs. The sensor experiences from a less resistive state to a more resistive one, resulting in an increased resistance change, which is responsible for the enhanced sensing performance for oxidizing gases with the ZnO/$SnO_2$ HSs. On the contrary, when reducing gas is supplied (Fig. 9b$_2$), the captured electrons are released, and the depletion layer becomes narrow. However, since the depletion layer has already been shortened by the electron transfer due to the n–n heterojunction with different work functions, the change of sensor resistance is decreased, leading to a smaller sensor response.[20] This is the reason why the ZnO/$SnO_2$ HSs exhibit increased and decreased sensor responses respectively for oxidizing and reducing gases.

Interestingly, as previously reported,[20,38] gas sensors developed by $SnO_2$–ZnO core–shell (C–S) nanofibers or nanowires exhibit opposite sensing performance, showing increased response for reducing gases and decreased response for oxidizing gases. In C–S structures, the model suggests that as the shell thickness increases, the dominant electrical transport pathway is localized from the core ($SnO_2$) to the shell layer (ZnO). When the shell thickness increases to be comparable to the Debye length of the shell material, the shell layer is completely depleted in air due to the chemisorption of oxygen species, resulting in a relatively high initial resistance. If the reducing gas is supplied, a large amount of electrons will return to the shell layer, leading to a low sensor resistance. The process from a more resistive state to a less one contributes to a large response. While for oxidizing gases, the depleted shell layer can hardly release free electrons to further adsorb gas molecules, only causing a small resistance change. In our case, the ZnO NPs are dispersively attached on the surface of $SnO_2$ NTs, not forming a continuous conducting shell, and the transport pathway is still confined to the $SnO_2$ NTs. Duo to electron transfer from ZnO NPs to $SnO_2$ NTs at the interface, the $SnO_2$ NTs become electron accumulated, beneficial to adsorb oxidizing gases, leading to an enhanced sensor response. The opposite sensing performances caused by the $SnO_2$–ZnO C–S structures and the ZnO/$SnO_2$ HSs demonstrate that the structure of heterojunctions can tremendously impact the sensing properties of sensor devices.

# 4. Conclusions

In summary, the ZnO nanoparticle-loaded electrospun $SnO_2$ nanotube n–n HSs were synthesized by electrospinning combined with facile thermal decomposition. The sensing properties of the pristine $SnO_2$ NTs and ZnO/$SnO_2$ HSs were investigated toward the representative oxidizing ($NO_2$) and reducing ($H_2$, CO) gases. The response of ZnO/$SnO_2$ HSs is 30.84 for 5 ppm $NO_2$, six times higher than that of $SnO_2$ NTs (5.09). While for 50 ppm $H_2$, the response of ZnO/$SnO_2$ HSs (1.44) becomes nearly one-fifth of the $SnO_2$ NTs (6.89). Results indicate that ZnO/$SnO_2$ HSs exhibit selectively enhanced and diminished sensing performances respectively for oxidizing and reducing gases. These phenomena are closely associated with the modulation of the local depletion layer on surface of $SnO_2$ NPs caused by charge transfer at the heterojunctions due to work function difference. A modified grain boundary-controlled sensing mechanism is proposed to describe charge transport in sensing layers based on the contact potential barriers between nanoparticles. Our study indicates that the selection of material system and their synergism are keys to the effective design of gas sensors with semiconducting metal oxide HSs.

# Acknowledgements

This work was supported by the fund from the Science and Technology on Plasma Physics Laboratory at Research Center of Laser Fusion, CAEP and the Science and Technology Development Fund of CAEP (2014A0302014).

# References

1 N. Barsan, D. Koziej and U. Weimar, *Sens. Actuators, B*, 2007, **121**, 18–35.
2 A. Tricoli, M. Righettoni and A. Teleki, *Angew. Chem., Int. Ed.*, 2010, **49**, 7632–7659.
3 D. J. Wales, J. Grand, V. P. Ting, R. D. Burke, K. J. Edler, C. R. Bowen, S. Mintova and A. D. Burrows, *Chem. Soc. Rev.*, 2015, **44**, 4290–4321.
4 N. Shehada, G. Brönstrup, K. Funka, S. Christiansen, M. Leja and H. Haick, *Nano Lett.*, 2014, **15**, 1288–1295.
5 G. F. Fine, L. M. Cavanagh, A. Afonja and R. Binions, *Sensors*, 2010, **10**, 5469–5502.
6 A. Berna, *Sensors*, 2010, **10**, 3882–3910.
7 A. Ponzoni, E. Comini, I. Concina, M. Ferroni, M. Falasconi, E. Gobbi, V. Sberveglieri and G. Sberveglieri, *Sensors*, 2012, **12**, 17023–17045.
8 http://www3.epa.gov/ttn/naaqs/criteria.html.
9 S.-W. Choi, A. Katoch, J.-H. Kim and S. S. Kim, *ACS Appl. Mater. Interfaces*, 2014, **6**, 17723–17729.
10 S.-W. Choi and S. S. Kim, *Sens. Actuators, B*, 2012, **168**, 8–13.
11 P. Rai, Y.-S. Kim, H.-M. Song, M.-K. Song and Y.-T. Yu, *Sens. Actuators, B*, 2012, **165**, 133–142.
12 X.-j. Wang, W. Wang and Y.-L. Liu, *Sens. Actuators, B*, 2012, **168**, 39–45.

 

13 D. J. Yang, I. Kamienchick, D. Y. Youn, A. Rothschild and I. D. Kim, *Adv. Funct. Mater.*, 2010, **20**, 4258–4264.
14 H. W. Kim, S.-W. Choi, A. Katoch and S. S. Kim, *Sens. Actuators, B*, 2013, **177**, 654–658.
15 G. Lu, L. E. Ocola and J. Chen, *Adv. Mater.*, 2009, **21**, 2487–2491.
16 M. Mashock, K. Yu, S. Cui, S. Mao, G. Lu and J. Chen, *ACS Appl. Mater. Interfaces*, 2012, **4**, 4192–4199.
17 D. R. Miller, S. A. Akbar and P. A. Morris, *Sens. Actuators, B*, 2014, **204**, 250–272.
18 D. Neamen, *Semiconductor physics and devices*, McGraw-Hill, Inc., 2002.
19 S. Sen, P. Kanitkar, A. Sharma, K. Muthe, A. Rath, S. Deshpande, M. Kaur, R. Aiyer, S. Gupta and J. Yakhmi, *Sens. Actuators, B*, 2010, **147**, 453–460.
20 S.-W. Choi, A. Katoch, G.-J. Sun, J.-H. Kim, S.-H. Kim and S. S. Kim, *ACS Appl. Mater. Interfaces*, 2014, **6**, 8281–8287.
21 J. Huang and Q. Wan, *Sensors*, 2009, **9**, 9903–9924.
22 M. J. Spencer, *Prog. Mater. Sci.*, 2012, **57**, 437–486.
23 R. Ab Kadir, Z. Li, A. Z. Sadek, R. Abdul Rani, A. S. Zoolfakar, M. R. Field, J. Z. Ou, A. F. Chrimes and K. Kalantar-zadeh, *J. Phys. Chem. C*, 2014, **118**, 3129–3139.
24 S. Bai, S. Chen, Y. Zhao, T. Guo, R. Luo, D. Li and A. Chen, *J. Mater. Chem. A*, 2014, **2**, 16697–16706.
25 A. Katoch, S.-W. Choi and S. S. Kim, *Nanotechnology*, 2014, **25**, 455504.
26 Q. Qi, P.-P. Wang, J. Zhao, L.-L. Feng, L.-J. Zhou, R.-F. Xuan, Y.-P. Liu and G.-D. Li, *Sens. Actuators, B*, 2014, **194**, 440–446.
27 S.-W. Choi, J. Zhang, K. Akash and S. S. Kim, *Sens. Actuators, B*, 2012, **169**, 54–60.
28 Z. Wang, Z. Li, T. Jiang, X. Xu and C. Wang, *ACS Appl. Mater. Interfaces*, 2013, **5**, 2013–2021.
29 L. Xu, R. Zheng, S. Liu, J. Song, J. Chen, B. Dong and H. Song, *Inorg. Chem.*, 2012, **51**, 7733–7740.
30 B.-H. Jang, O. Landau, S.-J. Choi, J. Shin, A. Rothschild and I.-D. Kim, *Sens. Actuators, B*, 2013, **188**, 156–168.
31 Y. Huang, Y.-E. Miao, L. Zhang, W. W. Tjiu, J. Pan and T. Liu, *Nanoscale*, 2014, **6**, 10673–10679.
32 X. Zhao, P. Wang, Y. Gao, X. Xu, Z. Yan and N. Ren, *Mater. Lett.*, 2014, **132**, 409–412.
33 K. Diao, M. Zhou, J. Zhang, Y. Tang, S. Wang and X. Cui, *Sens. Actuators, B*, 2015, **219**, 30–37.
34 L. Wang, Z. Lou, J. Deng, R. Zhang and T. Zhang, *ACS Appl. Mater. Interfaces*, 2015, **7**, 13098–13104.
35 T. Kida, S. Fujiyama, K. Suematsu, M. Yuasa and K. Shimanoe, *J. Phys. Chem. C*, 2013, **117**, 17574–17582.
36 Y.-F. Sun, S.-B. Liu, F.-L. Meng, J.-Y. Liu, Z. Jin, L.-T. Kong and J.-H. Liu, *Sensors*, 2012, **12**, 2610–2631.
37 C. Wang, L. Yin, L. Zhang, D. Xiang and R. Gao, *Sensors*, 2010, **10**, 2088–2106.
38 A. Katoch, S.-W. Choi, G.-J. Sun and S. S. Kim, *J. Mater. Chem. A*, 2013, **1**, 13588–13596.
39 K. Sahner and H. Tuller, *J. Electroceram.*, 2010, **24**, 177–199.
40 S. J. Gregg and K. S. W. Sing, *Adsorption, Surface Area, and Porosity*, Academic Press, London, 1991.
41 S.-W. Choi, J. Y. Park and S. S. Kim, *Chem.–Eng. J.*, 2011, **172**, 550–556.
42 S.-W. Choi, J. Y. Park and S. S. Kim, *J. Mater. Res.*, 2011, **26**, 1662–1665.
43 C. Jin, S. Park, H. Kim and C. Lee, *Sens. Actuators, B*, 2012, **161**, 223–228.
44 C. Xu, J. Tamaki, N. Miura and N. Yamazoe, *Sens. Actuators, B*, 1991, **3**, 147–155.
45 N. Barsan and U. Weimar, *J. Electroceram.*, 2001, **7**, 143–167.
46 S. M. Sze and K. K. Ng, *Physics of semiconductor devices*, John Wiley & Sons, 2006.
47 H. Ogawa, M. Nishikawa and A. Abe, *J. Appl. Phys.*, 1982, **53**, 4448–4455.
48 D. C. Look, J. W. Hemsky and J. Sizelove, *Phys. Rev. Lett.*, 1999, **82**, 2552.
49 Ü. Özgür, Y. I. Alivov, C. Liu, A. Teke, M. Reshchikov, S. Doğan, V. Avrutin, S.-J. Cho and H. Morkoc, *J. Appl. Phys.*, 2005, **98**, 041301.